

Twist versus heterostrain control of optical properties of moiré exciton minibands

Huiyuan Zheng, Dawei Zhai, and Wang Yao

*Department of Physics and Guangdong-Hong Kong Joint Laboratory of Quantum Matter,
The University of Hong Kong, Hong Kong, China and
HKU-UCAS Joint Institute of Theoretical and Computational Physics at Hong Kong, China*
(Dated: October 5, 2021)

We investigate the optical properties of interlayer excitons in heterobilayer transition metal dichalcogenides where moiré pattern is introduced by heterostrain, in comparison with that introduced by twisting (and/or lattice mismatch). Besides being a cause of the moiré texture, strain also effectively introduces a constant gauge potential on either electron or hole, which shifts the dispersion of kinetic energy with respect to the excitonic crystal momenta in the moiré superlattices. This leads to distinct exciton mini-band dispersions and light coupling properties from the twisting induced moiré, even if the excitonic moiré superlattice potentials have the similar real-space profile for the two cases. For strain that breaks the three-fold rotational symmetry at the atomic scale, the exciton wave packets trapped at the superlattice potential minima have elliptically polarized valley optical selection rules, in contrast to the circularly polarized ones in the twisting moiré. We investigate the evolution of the excitonic mini-bands and the optical dipoles of the bright states inside the light cones with the decrease of the moiré periodicity, upon which the excitonic wave functions evolve from localized wave packets to the extended Bloch states. Furthermore, moiré exciton properties under the interplay of twisting and heterostrain are also discussed.

I. INTRODUCTION

Atomically thin group-VIB transition metal dichalcogenides (TMDs) have emerged as a class of two-dimensional (2D) semiconductors with exciting optical properties. The monolayers feature direct band gaps in the visible frequency range^{1,2}, with band edges located at the degenerate \mathbf{K} and $-\mathbf{K}$ corners of the hexagonal Brillouin zone (BZ), which constitute the valley degree of freedom. Optical properties of TMDs are dominated by the hydrogen-like bound states of the electron and hole at the valleys, where strong Coulomb interaction leads to exceptionally large exciton binding energies³. As the monolayers are only bounded by weak van der Waals (vdW) interactions, heterostructures of different TMDs can be flexibly engineered without the requirement of lattice matching, which allows vast opportunities to engineer and extend optoelectronic properties. TMD heterobilayers typically feature the type-II alignment where electron and hole energetically favor the two opposite layers. Interlayer excitons (IXs) with the layer separation of the electron and hole ingredients therefore becomes the lowest energy configuration that can dominate the photoluminescence⁴. Compared with monolayer excitons, IXs in TMD bilayers exhibit ultralong recombination lifetime and spin-valley lifetime due to the reduced electron-hole wave function overlap, and electrically tunable resonance and strong dipolar interaction due to the permanent electrical dipole, providing rich possibilities in optoelectronic applications⁴⁻⁹.

Without the requirement of lattice matching, small differences in lattice constant and crystalline orientation lead to the formation of moiré patterns, i.e. spatial modulation on atomic registries from the interference of two mismatched atomic lattices. The sensitive dependence of electronic structures on the atomic stacking reg-

istries therefore results in the spatial variation in the local band gap in heterobilayers¹⁰. The moiré-patterned band gap corresponds to the spatial modulation of IX energy, which can be tuned electrically by means of Stark effect, while the spatial profile can be engineered through the variation of twisting angles¹¹. IXs in such moiré potential can be exploited in two functioning regimes: (i) excitonic emitters localized in trap arrays in relatively large moiré; and (ii) excitonic superlattices in relatively small moiré, where exciton hopping leads to formation of mini-bands¹². Evidences of moiré excitons in both regimes are reported with distinct spectroscopic features in the various heterobilayers¹³⁻¹⁸. However, a systematic analysis of how the moiré exciton optical properties vary between the two regimes is still lacking, which is one of the issues that we address in this work.

On the other hand, moiré patterns can also be created by applying layer-dependent strain (i.e. heterostrain) to lattice matched bilayers¹⁹⁻²¹. In particular, under a volume preserving strain, the bilayer moiré will exhibit a large-scale interference pattern nearly indistinguishable from that introduced by twisting and/or lattice mismatch (Fig. 1a). Compared to twisting, the heterostrain approach allows in situ tunability of the moiré, where the periodicity can in principle be controlled via substrates mechanically, thermally or piezoelectrically²²⁻²⁶. Besides, strain can be unintentionally introduced due to unavoidable deformation in fabrications of moiré superlattices, where the interplay of uniaxial strain and twisting can lead to dramatic elongation of the moiré towards one-dimensional structure. Linearly polarized IX photoluminescence in the strain elongated moiré traps has been reported in TMDs heterobilayers²⁷. In the heterostrained moiré superlattices, distinguished IX properties can be expected as compared to the twisting induced ones. A qualitative picture is that the breaking of rota-

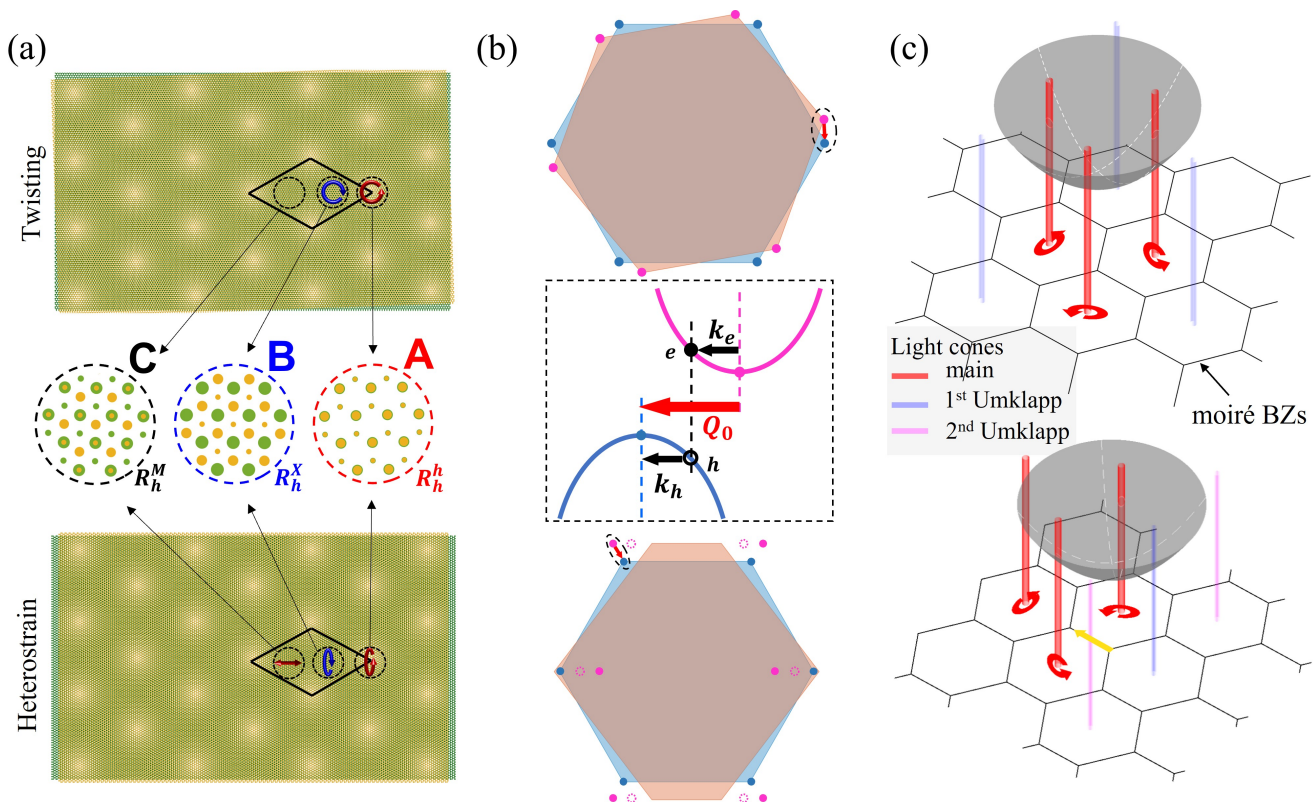


FIG. 1. Comparison between interlayer excitons in twisting and heterostrain induced moiré patterns. (a) Real space configuration of bilayers subject to twisting (upper panel) or volume-preserving heterostrain (lower panel). Black rhombus depicts a moiré supercell. The in-plane polarizations of a \mathbf{K} valley exciton at different high symmetry locations (dashed circles) are schematically shown. At R_h^h and R_h^X stacking locals, circular (elliptical) polarization is allowed in the twisted (heterostrained) moiré. At the R_h^M stacking local in-plane linear polarization is forbidden (allowed) in twisted (heterostrained) moiré. (b) Mismatched monolayer BZs of twisted and heterostrained bilayers. The blue and red color represent the bottom and top layer, respectively. Blue (magenta) solid dots are Dirac points of the bottom (top) layer. For the strain case, we show both the Dirac point locations with (solid dots) and without (empty dots) considering the strain induced gauge potential. Red arrows mark the center-of-mass kinematic momentum of a bright IX, which correspond to the mismatch of the Dirac points in the two layers. The middle dashed box illustrates the various momenta in a bright IX with electron and hole from each layer. (c) Distinct distribution of light cones (cylinders) with respect to the IX kinetic energy dispersion (gray parabola) in the twisted (upper panel) and heterostrained (lower panel) moiré. Compared to twisted moiré, two major differences are noted in heterostrained moiré: (1) Exchange of the elliptical polarization at the three main light cones; (2) Overall shift of the light cone locations (yellow arrow) with respect to the kinetic energy dispersion.

tional symmetry can change optical selection rules from circular to linear polarization, but a systematic study of how this happens has not been carried out yet.

In this work we systematically study the mini-band dispersion and optical properties of IXs in heterostrain induced moiré, in comparison with those in the moiré induced by twisting of various angles. The two types of moiré patterns have the valley mismatch between electron and hole in a different manner, which results in distinct distribution of light cones with respect to the exciton kinetic energy dispersion (Fig. 1c). The broken rotational symmetry in the strain induced moiré manifests as the exchange in positions of the main light cones with different polarized dipoles. Besides, the strain also introduces a constant gauge potential on either electron or hole, which shifts the dispersion of exciton with respect to its crystal momenta in the moiré superlattice, lead-

ing to dramatic changes of kinetic energies at the main and Umklapp light cones. Upon the band folding by the moiré superlattice potential, the mini-band dispersion, wave function spatial profile, and optical properties are totally distinct, even if moiré superlattice potentials have the similar real-space profile for the two cases. We also show the evolution of the excitonic mini-bands and the optical dipoles of the bright states inside the light cones with the decrease of moiré periodicity, during which the excitonic wave functions evolve from localized wave packets to extended Bloch states. We explore various types of strain configurations and the interplay of twisting and heterostrain, and provide comprehensive diagrams on the optical properties of moiré IXs in the strain-parameter space. These studies form the basis of strain and twisting engineering of moiré exciton optical properties for potential photonic applications.

The rest of the paper is organized as the following. In Sec. II we give a brief description of the IX momentum eigenstates, the relation of kinetic energy with respect to its crystal momentum that can be defined from the superlattice Bloch function form, as well as the moiré potential that couples the momentum eigenstates. In Sec. III, IXs in twisted heterobilayer are first investigated with the variation of twisting angles to explore the transition between small and large moiré regimes. Sec. IV presents the strained moiré IXs in comparison with the twisting case. The change of BZ geometry and the effective gauge potential from strain are first introduced, and the resultant consequences on the light cone distribution, mini-band dispersion, wave functions, and optical properties are analysed. At last, we briefly discuss properties of IXs under the interplay of twisting and strain.

II. IX MOMENTUM EIGENSTATE AND MOIRÉ POTENTIAL

A. Exciton momentum eigenstates in misaligned bilayers

TMDs²⁸ possess a hexagonal BZ with massive Dirac cones located at the corners $\tau\mathbf{K}$ and $\tau = \pm 1$ is the valley index. Excitons in TMDs exhibit spin-valley locking due to the large spin-orbit splitting. For TMD heterobilayers with type-II band alignment, IXs are composed of electrons and holes located at $\tau'\mathbf{K}'$ and $\tau\mathbf{K}$ valleys in different layers. Here we use prime to denote quantities from the upper layer. Apart from misalignment of the Dirac cones in energy, locations of Dirac cones in momentum space are affected by the configuration of the bilayer. In a twisted bilayer, Dirac cones in the upper layer are rotated with respect to those in the lower layer (Fig. 1b upper panel). In a strained bilayer, Dirac cones are first shifted away from the corners of the distorted BZ (red shaded area in Fig. 1b lower panel) due to the breaking of three-fold rotational symmetry (empty pink dots). Moreover, the Dirac cones are further translated by a pseudogauge potential caused by changes of the hopping energy (from empty to solid pink dots), which will be discussed in Sec. IV A.

Using Bloch wave functions of a pair of electron and hole from each individual layer, $\psi_{\mathbf{k}_e}^e(\mathbf{r}_e)$ and $\psi_{\mathbf{k}_h}^h(\mathbf{r}_h)$, one can construct the IX momentum eigenstate. Since Coulomb interaction conserves the center-of-mass (COM) momentum \mathbf{Q} of electron and hole, it is a good quantum number to characterize the IX momentum eigenstate²⁹:

$$\begin{aligned} X_{\tau'\tau,\mathbf{Q}}(\mathbf{R}, \mathbf{r}_{eh}) &= \sum_{\Delta\mathbf{Q}} \Phi(\Delta\mathbf{Q}) \psi_{\tau'\mathbf{K}'+\frac{m_e}{M_0}\mathbf{Q}+\Delta\mathbf{Q}}^e \psi_{\tau\mathbf{K}-\frac{m_h}{M_0}\mathbf{Q}+\Delta\mathbf{Q}}^{h*} \\ &= e^{i(\mathbf{Q}+\tau'\mathbf{K}'-\tau\mathbf{K})\cdot\mathbf{R}} U_{\tau'\tau,\mathbf{Q}}(\mathbf{R}, \mathbf{r}_{eh}) \end{aligned} \quad (1)$$

In the above, the coordinates and momenta of electrons

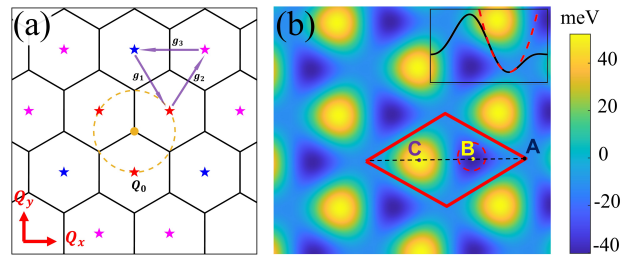


FIG. 2. (a) Light cones in the extended BZ scheme for a twisted moiré. The black hexagons denote the moiré BZs, purple arrows mark $\mathbf{g}_1, \mathbf{g}_2$, and \mathbf{g}_3 . Red stars stand for main light cones, and blue/pink stars represent the 1st/2nd Umklapp light cones. The origin $\mathbf{Q} = 0$ is marked by the brown dot and the brown circle is the equi-energy ring from main light cones. (b) The moiré potential landscape for R-type WSe₂/MoSe₂, where red rhombus marks a moiré supercell. A, B, and C label three high symmetry locals. The potential inside the red dashed circle can be approximated as a harmonic trap in the small twist angle regime. Upper right inset: Cross-section of the potential along the long axis of the supercell (black solid curve) and the harmonic approximation (red dashed curve).

and holes have been replaced by their COM and relative motion counterparts $\mathbf{R} = \frac{m_e}{M_0}\mathbf{r}_e + \frac{m_h}{M_0}\mathbf{r}_h$, $\mathbf{r}_{eh} = \mathbf{r}_e - \mathbf{r}_h$, $\mathbf{k}_e = \tau'\mathbf{K}' + \frac{m_e}{M_0}\mathbf{Q} + \Delta\mathbf{Q}$, and $\mathbf{k}_h = \tau\mathbf{K} - \frac{m_h}{M_0}\mathbf{Q} + \Delta\mathbf{Q}$ with $M_0 = m_e + m_h$ the exciton mass, $\Delta\mathbf{Q}$ the relative momentum, and $\Phi(\Delta\mathbf{Q})$ the relative motion wave function. The COM momentum \mathbf{Q} is also called the *kinetic momentum* since it is associated with the IX's kinetic energy $\hbar^2\mathbf{Q}^2/2M_0$. $U_{\tau'\tau,\mathbf{Q}}(\mathbf{R}, \mathbf{r}_{eh})$ in the last line of Eq. (1) is a periodic function built from the periodic parts of the electron and hole's Bloch wave functions²⁹. This makes the IX momentum eigenstate of the Bloch type, where $\mathbf{k}_c = \mathbf{Q} + \tau'\mathbf{K}' - \tau\mathbf{K}$ plays the role of *crystal momentum*. In the following, we will focus on the $\tau = \tau' = +$ valley in R-stacking (or parallel) heterobilayers. The other valley is related by time-reversal symmetry. Also, a consistent coordinate system has been chosen throughout the work, i.e. the zigzag (armchair) crystalline direction as x (y) axis.

Note that the crystal momentum \mathbf{k}_c and kinetic momentum \mathbf{Q} are different for IXs in the moiré. This contrasts with intralayer excitons in monolayers, or IXs in aligned lattice-matched heterobilayers, where the two momenta are identical due to $\mathbf{K}' - \mathbf{K} \equiv 0$. When an exciton is converted into a photon, momentum conservation requires that the crystal momentum satisfies $\mathbf{k}_c \approx 0$. Therefore, intralayer excitons in monolayers or IXs in aligned lattice-matched heterobilayers have vanishing kinetic momentum (brown dot in Fig. 2a). In contrast, bright IXs in the moiré have finite kinetic momentum $\mathbf{Q}_{lc} = \mathbf{K} - \mathbf{K}' + \mathbf{G}$ (stars in Fig. 2a), where \mathbf{G} denotes the moiré reciprocal lattice vector. \mathbf{Q}_{lc} defines the location of moiré light cones, inside which the direct conversion with photon is permitted (Fig. 1b).

Moiré IX momentum eigenstates in various light cones possess distinct optical dipoles coupled to different elliptically polarized light³⁰ (Fig. 1c). In the case of twisted heterobilayer moiré, the three equivalent innermost light cones are located at $\mathbf{Q}_0 = \mathbf{K} - \mathbf{K}'$, $C_3\mathbf{Q}_0$, and $C_3^2\mathbf{Q}_0$ (red stars in Fig. 2a, C_3 denotes three-fold rotation). These are the main light cones, in which the momentum eigenstates hold dominant optical dipoles. Farther away are the Umklapp light cones, which represent the Umklapp recombination process with much weaker dipoles. Such categorization can also be applied to strained heterobilayer moiré, although three-fold rotational symmetry is broken.

B. Moiré potential

Moiré patterns from the misaligned bilayers exhibit spatially modulated local atomic registry that repeats in a much larger scale than the monolayer lattice constant. Different local atomic configurations in a moiré render local-to-local variation on the interlayer vdW interaction, forming a lateral modulation on the local band gap and interlayer distance²⁹. The IX thus experiences a moiré potential, which can be modeled by^{12,31–33}

$$V(\mathbf{R}) = \sum_{n=1}^3 2V_0 \cos(\mathbf{g}_n \cdot \mathbf{R} - \varphi), \quad (2)$$

where \mathbf{g}_1 , \mathbf{g}_2 , and $\mathbf{g}_3 = -\mathbf{g}_1 - \mathbf{g}_2$ are the primitive reciprocal lattice vectors of the moiré superlattice separated by 120° (purple arrows in Fig. 2a). The information of the moiré profile is contained in the reciprocal lattice vectors, which vary for different moiré superlattices (e.g. the two cases in Fig. 1). Values of V_0 and φ depend on materials and their stacking configuration^{32,34}. For example, $V_0 = 9.122$ meV and $\varphi \approx 0.57\pi$ for R-type WSe₂/MoSe₂ heterobilayer^{12,33}. The potential profile in a twisted moiré superlattice is shown in Fig. 2b. Each potential minimum (B) is connected with three saddle points (A) and three maxima (C). The three locals A, B, and C correspond to R_h^h , R_h^X , and R_h^M high symmetry stacking registries, respectively (Fig. 1a). Here, R_h^μ denotes R-type stacking, with the μ site of the electron layer vertically aligned with the hexagon center (h) of the hole layer. M and X represent metal and chalcogen atoms.

The momentum space Hamiltonian describing the moiré exciton Bloch states in the slowly varying moiré potential reads^{12,33}

$$H = \sum_l \left[\left(E_X + \frac{\hbar^2 |\mathbf{Q}_l|^2}{2M_0} \right) |\mathbf{Q}_l\rangle \langle \mathbf{Q}_l| \right] + \sum_l \left[\sum_{n=1}^3 (V_0 |\mathbf{Q}_l + \mathbf{g}_n\rangle \langle \mathbf{Q}_l| + h.c.) \right] \quad (3)$$

where $|\mathbf{Q}_l\rangle$ is the momentum eigenstate in the l th mini BZ, $E_X \approx 1.40$ eV and is tunable with electric field. The

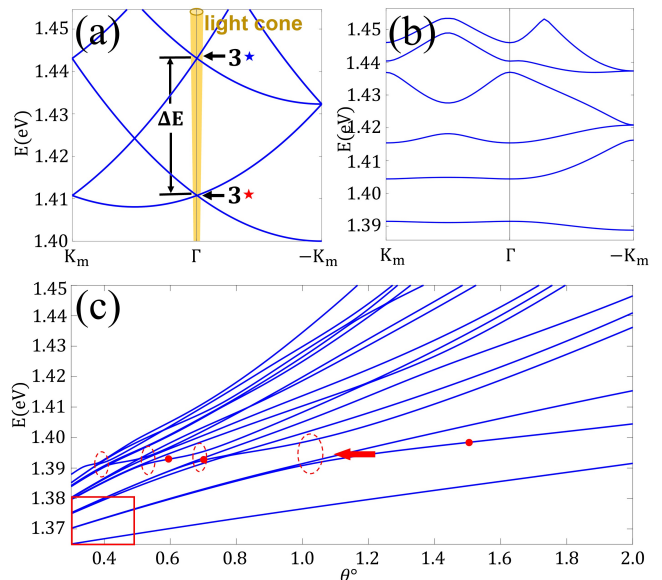


FIG. 3. Dispersion relations of IX in twisted heterobilayer moiré. (a) The dispersion in the mini BZ at $\theta = 2^\circ$ in the absence of moiré potential. $\pm K_m$ are the mini BZ corners. There are two degenerate points at Γ , which consist of three main light cones and three 1st Umklapp light cones, respectively. The yellow cone stands for the light cone with very sharp slope, so only the states near Γ point can couple to light directly. (b) The dispersion in the presence of moiré potential. Gaps are opened at the degenerate points in (a). (c) The first 16 energy levels at Γ with the variation of twist angle from 0.3° to 2.0° . States inside the red box exhibit equal energy spacing and linear scaling. There is a plateau state around 1.39 eV, whose energy barely changes with θ . Red ellipses mark the hybridization of this state with other states forming anti-crossings. The red dots mark the states whose wave functions are shown in Fig. 4b.

second line illustrates that each momentum eigenstate is coupled to six neighboring states with momentum difference $\pm \mathbf{g}_n$, which will lead to the formation of mini-bands.

III. INTERLAYER EXCITONS IN TWISTED HETEROBILAYER MOIRÉ

We first investigate IXs in twisted heterobilayer moiré with various twisting angles. We take R-type WSe₂/MoSe₂ bilayer and consider the spin singlet moiré exciton²⁹.

A. Energy dispersion

Figs. 3a,b show the IX dispersion along $-K_m - \Gamma - K_m$ in the mini BZ without and with the moiré potential at twist angle $\theta = 2^\circ$. In the absence of moiré potential, the dispersion only comes from the parabolic kinetic energy. \mathbf{Q}_{lc} , where light cones reside, are folded onto the Γ

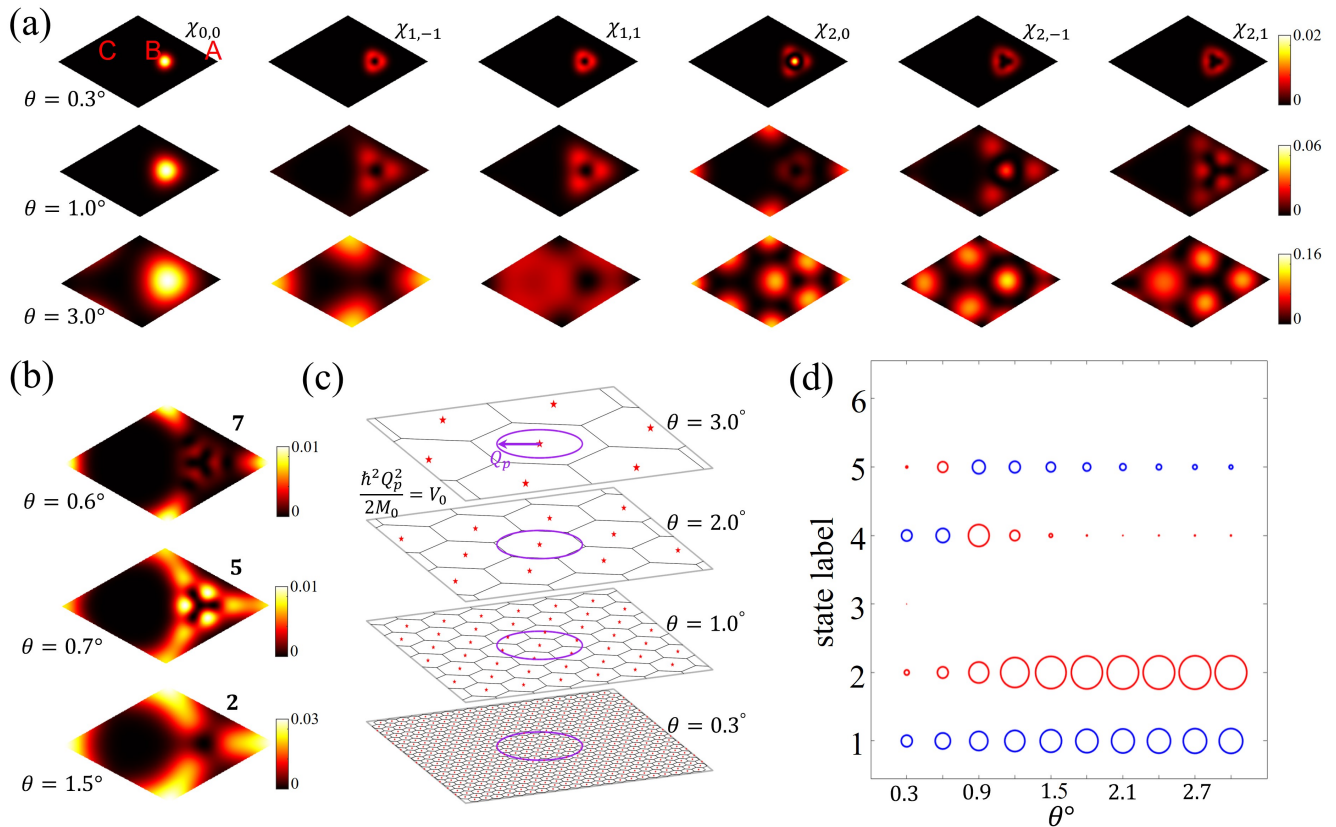


FIG. 4. Wave function distribution for the low energy exciton mini-bands in twisted heterobilayer moiré of various twist angles. (a) Wave function densities of the first 6 states at $\theta = 0.3^\circ, 1.0^\circ$, and 3.0° . Wave functions at small twist angle possess harmonic forms, where the orbital symmetry is labeled on the first row. (b) Evolution of the plateau state with twist angle (c.f. Fig. 3c, where the corresponding states are marked by red dots). It mainly distributes around A locals and will hybridize with states located around B point if their energies intersect ($\theta = 0.7^\circ$). (c) The effective coupling range dictated by moiré potential strength. Light cone (red stars) distribution in the extended mini-BZs is shown at different twist angles, where the circle has radius $Q_p \equiv \frac{\sqrt{2m}V_0}{\hbar}$, subscript p stands for moiré potential. Momentum eigenstates within the range characterized by Q_p are strongly coupled by the moiré potential. (d) In-plane polarization of moiré excitons for $\theta = 0.3^\circ$ to 3.0° . Red/blue color stands for right/left circular polarization, circle size stands for dipole amplitude.

point. The first energy level at Γ is three-fold degenerate consisting of three main light cones (red stars in Fig. 2a). The second level is composed of three 1st Umklapp light cones (blue stars in Fig. 2a). In the presence of moiré potential, degeneracy is broken with gap opening. If the energy separation between the two levels is smaller than the potential energy, i.e., $\Delta E < V_0$ (Fig. 3a), coupling between main and 1st Umklapp light cones will occur³³.

With the variation of twist angle, energy levels at the Γ point will evolve and certain states may mix (Fig. 3c). The kinetic momentum \mathbf{Q} increases approximately linearly with θ , thus the kinetic energy evolves with $|\mathbf{Q}|^2 \sim \theta^2$. In the small angle regime ($\theta < 1.5^\circ$), the separation of kinetic energy between the main and 1st Umklapp light cones is smaller than or comparable to the moiré potential strength, i.e., $\Delta E \lesssim V_0$. Thus, strong coupling between main and Umklapp light cones is expected. When twist angle is large ($\theta \gtrsim 3.0^\circ$), $\Delta E > V_0$, the main and Umklapp light cones are effectively decoupled.

Several interesting features can be identified in the evo-

lution of energy levels with twist angle. First, the lowest a few levels exhibit equal spacing and scale linearly when θ is small (red box in Fig. 3c). Second, there is a plateau state around 1.39 eV whose energy is robust against variation of θ . It corresponds to the 16th state at $\theta = 0.35^\circ$ and becomes the 2nd when $\theta > 1.1^\circ$ since the other levels increase with θ and rise to higher energies.

B. Wave function distribution

It is also interesting to look at the wave function distribution for the first a few states at Γ point (Fig. 4a). One can notice that the first a few states are localized around potential minima (B point) at small angles, e.g., $\theta = 0.3^\circ$. Particularly, profiles of the first a few states at small angles are analogous to the eigenstates of a two-dimensional harmonic oscillator with the constraint of three-fold rotational symmetry. Consequently, we can label the states as $\chi_{n,l}$, where n is the principal quantum number, and

l is the angular momentum quantum number modulo 3 (1st row of Fig. 4a). These features and the scaling of energy levels discussed in the previous paragraph can be easily understood by realizing that the low energy IXs are trapped at the potential minima (B point), which can be well approximated as a harmonic oscillator potential (Fig. 2b inset) $V(\rho) \approx 1.47V_0 (4\pi^2\rho^2/a_m^2 - 3)$ with ρ the radial distance measured from B point and a_m the moiré period. Since the frequency of the harmonic oscillator $\omega \propto a_m^{-1} \propto \theta$, one recovers the equal spacing and linear in θ scaling at low energies. When θ is enlarged, high symmetry locals in the moiré shrink rapidly and the hopping between adjacent trapping sites in different supercells emerge, thus wave functions start to spread (2nd row of Fig. 4a). For even larger twist angles, the harmonic oscillator approximation breaks down, for example, the first three states mainly occupy B, A, C locals respectively when $\theta = 3.0^\circ$ (3rd row of Fig. 4a). Such wave function evolution can also be understood from a momentum space perspective. Momentum eigenstates in neighboring moiré BZs are coupled by moiré potential, whose strength can be characterized by an effective momentum length Q_p satisfying $\hbar^2 Q_p^2 / 2M_0 = V_0$. The purple circles in Fig. 4c delimit the region defined by the effective momentum. At small twist angles, the circle covers a large number of light cones. Many momentum eigenstates participate in constructing a moiré exciton eigenstate, the strong coupling among which yields a localized wave function. At large twist angles, the separation between light cones is increased, rendering a dramatically reduced number of light cones inside this circle. The wave functions of the excitons are built with less coupled momentum eigenstates and inherit their extended Bloch wave nature.

Now let us look at some features of the plateau state around 1.39 eV. It corresponds to the second state when $\theta > 1.1^\circ$, while its ordering changes with smaller θ and hybridization with other states occur around certain angles. It mainly distributes around the A high symmetry locals at most twist angles as shown by the top and bottom panels of Fig. 4b. This helps understand its insensitivity to variation of θ : Excitons residing around A locals experience a rather flat potential landscape with magnitude around $-V_0$, whose energy barely changes with the size of moiré. Therefore, the plateau state exhibits an almost constant energy around $E_X - V_0 \approx 1.39$ eV. At twist angles where the energy level of the plateau state intersects with others, strong hybridization occur between it and those states located around B with the appearance of avoided crossings as marked by the dashed circles in Fig. 3c. For example, at $\theta = 0.7^\circ$ (middle panel of Fig. 4b), the plateau state hybridizes with an extended $W_{2,-1}$ state rendering large densities around the B local.

C. Optical properties

Next we investigate the optical properties of twist moiré IXs at various angles. We focus on the first six states at Γ (Fig. 3b). One finds that all the states couple with circularly polarized light except the 3rd and 6th states, whose in-plane dipole vanishes (Fig. 4d). Red/blue color represents right/left circular direction, the size of circles denote the dipole amplitude. When $\theta < 1.5^\circ$, $\Delta E \lesssim V_0$ and the effective momentum Q_p that characterizes the range of moiré potential covers many light cones (Fig. 4c), states in the main and 1st Umklapp light cones couple significantly. Thus, strong optical dipoles from main light cones and weak dipoles from Umklapp light cones are mixed, producing comparable dipole strengths for different states. The insensitivity of the plateau state energy against variation of θ is also reflected on optical properties. The switching of polarization in the 4th and 5th states from $\theta = 0.6^\circ$ to 0.9° is related to the reordering of plateau state— It corresponds to the 5th state at $\theta = 0.6^\circ$, then exchanges order with its neighbor and becomes the 4th state at $\theta = 0.9^\circ$. With the twist angle enlarged, the coupling between main and 1st Umklapp light cones becomes weaker. Optical dipoles of the first three states are mostly contributed by the three main light cones. The fourth to sixth states are mainly governed by the three 1st Umklapp light cones with much weaker dipole intensities. At $\theta = 3.0^\circ$, wave functions for the three lowest states with dominating dipoles are well separated (3rd row of Fig. 4a): The 1st to 3rd states are centered at B, A, and C locals, respectively. Consequently, A, B locals in the moiré supercells are coupled uniquely to the σ_+ , σ_- polarized light, respectively, and in-plane polarization is forbidden at C locals (Fig. 1a upper panel)^{12,29}. The 4th to 6th states have much wider spread, however, the location-dependent optical properties remain applicable. For instance, the 4th (5th) state contributes σ_+ (σ_-) light emitting at the A (B) local (among other places), although the intensity is much weaker.

The observed optical properties in both small and large angle regime can be understood through symmetry analysis. The photon polarization from optical recombination of moiré excitons depends on the rotational symmetry. At small twist angles, the photon polarization is dictated by symmetry of local orbitals of the wave functions (first row of Fig. 4a). The moiré exciton in a wide potential well can be approximated as a wave packet¹² $\chi_{n,l} = \sum_{\mathbf{Q}} e^{-i(\mathbf{Q}-\mathbf{Q}_0)\cdot\mathbf{R}_c} W_{n,l}(\mathbf{Q}) X_{\mathbf{Q}}$, where $W_{n,l}(\mathbf{Q})$ is the 2D harmonic envelope wave function constraint by three-fold rotational symmetry. Setting the wave packet center \mathbf{R}_c at the B point, the in-plane optical dipole \mathbf{D}_{\parallel} can be analyzed via

$$\begin{aligned} \hat{e}_+ \cdot \mathbf{D}_{\parallel} &\sim W_{n,l}(\mathbf{Q}_0) + e^{i\frac{2\pi}{3}} W_{n,l}(C_3\mathbf{Q}_0) + e^{i\frac{4\pi}{3}} W_{n,l}(C_3^2\mathbf{Q}_0) \\ \hat{e}_- \cdot \mathbf{D}_{\parallel} &\sim W_{n,l}(\mathbf{Q}_0) + W_{n,l}(C_3\mathbf{Q}_0) + W_{n,l}(C_3^2\mathbf{Q}_0) \end{aligned} \quad (4)$$

For example, at $\theta = 0.3^\circ$, $W_{0,0}(\mathbf{Q}) = W_{0,0}(Q)$ is a real function of Q (Fig. 4a). This yields $\hat{e}_+ \cdot \mathbf{D}_{\parallel} \sim$

$W_{0,0}(Q_0) + e^{i\frac{2\pi}{3}}W_{0,0}(Q_0) + e^{i\frac{4\pi}{3}}W_{0,0}(Q_0) = 0$, while $\hat{e}_- \cdot \mathbf{D}_{\parallel} \sim W_{0,0}(Q_0) + W_{0,0}(Q_0) + W_{0,0}(Q_0)$ is finite. By the same token, the above orbital optical selection rule determines that states with $l = 0$ emit σ_- light, states with $l = -1$ emit σ_+ light, while states with $l = 1$ have vanishing in-plane polarization, which is consistent with results of Fig. 4d (e.g., first column).

At large angles (e.g., $\theta = 3.0^\circ$), momentum eigenstates in neighboring BZs are weakly coupled, so wave functions become more extended. The optical dipoles instead depend on real-space atomic configurations. The electron and hole Bloch functions have distinct C_3 eigenvalues about different rotation centers (h center, chalcogen site, or metal site, Fig. 1a middle panel). Moiré excitons χ at different high symmetry locals have distinct rotation centers, thus they exhibit location-dependent C_3 transformations^{12,29}

$$C_3\chi_A = e^{-i\frac{2\pi}{3}}\chi_A, C_3\chi_B = e^{i\frac{2\pi}{3}}\chi_B, C_3\chi_C = \chi_C \quad (5)$$

Photons converted from such excitons possess the same symmetry. Since the first six states have specific rotational centers, moiré excitons in the large angle regime exhibit location-dependent optical selection rules as schematically shown in Fig. 1a.

IV. INTERLAYER EXCITONS IN HETEROSTRAINED MOIRÉ

In this section we consider IXs in moiré formed by various types of heterostrain³⁵ For simplicity, we assume that only the top layer is strained. We compare properties of IXs in strained moiré with those in the twisted case.

A. Strain effect

To characterize the IX in a moiré formed by heterostrain, first we give a brief introduction to the geometric and electronic effects of strain^{36–39}.

First, strain introduces geometric changes to the lattice structure (Fig. 1a lower panel). Such geometric variations shift the location of Dirac cones to $\tau(I + S)^{-1}\mathbf{K}$ (dashed pink circles in Fig. 1b lower panel), where I is the identity matrix and S is the strain tensor.

Apart from geometric effects on the crystalline structure, strain also modifies the hopping energy along different directions. In the limit of small strain, such variation can be captured by a pseudogauge potential in terms of strain tensor components

$$\mathbf{A} = \frac{\sqrt{3}}{2a}\beta(\epsilon_{xx} - \epsilon_{yy}, -2\epsilon_{xy})^T, \quad (6)$$

where β is a material-dependent parameter, for instance, $\beta \approx 2.30$ for WSe_2 ³⁸. Consequently, the two Dirac points in the monolayer BZ are further shifted oppositely (to

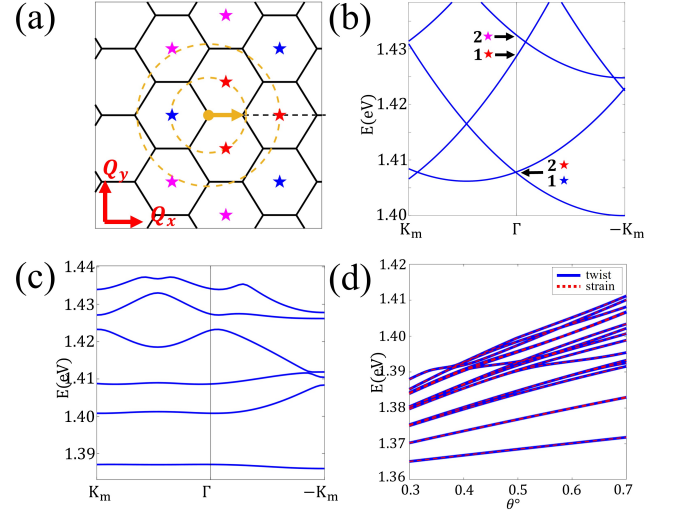


FIG. 5. (a) Light cone distribution in the moiré formed by volume-preserving strain along the zigzag direction. Black hexagons denote the moiré BZs. Red and blue/pink stars represent main and 1st/2nd Umklapp light cones. The brown dot, arrow and dashed circles represent the origin, gauge potential \mathbf{A} , and equi-energy rings, respectively. (b) The kinetic energy dispersion of heterostrained moiré excitons at $\epsilon = 3.0\%$. Three-fold degeneracies at Γ are broken due to strain. Composition of light cones for different levels at Γ are also labeled. (c) Dispersion of heterostrained moiré excitons in the presence of moiré potential. (d) Comparison of energy levels at Γ between twisted (blue) and heterostrained (red dashed) moiré excitons. Note that strain intensity has been converted into angles to facilitate the comparison (i.e. $\epsilon/\pi \times 180^\circ$).

respect time-reversal symmetry) by the pseudogauge potential towards

$$\tau\mathbf{D} = \tau(I + S)^{-1}\mathbf{K} - \tau\mathbf{A}, \quad (7)$$

as shown schematically from pink circles to pink dots in Fig. 1b lower panel. The first term represents the distorted Dirac points due to geometric distortion discussed in the previous paragraph. In contrast to the twisting case, the Dirac points are shifted away from the BZ corners.

B. Volume-preserving heterostrain

Here we consider volume-preserving strain^{40,41}, i.e., stretching the top layer along the zigzag direction while compressing it with the same extent in the perpendicular direction (Fig. 1a). The strain tensor reads $S = \text{diag}(\epsilon, -\epsilon)$, where ϵ is the strain strength. In this case, the large-scale moiré landscape resembles that of a twisted bilayer (Fig. 1a). This similarity also applies to the superlattice potentials based on the local approximation for long-period moiré (Appendix A). This allows us to focus first on the effects of the pseudo-gauge potential

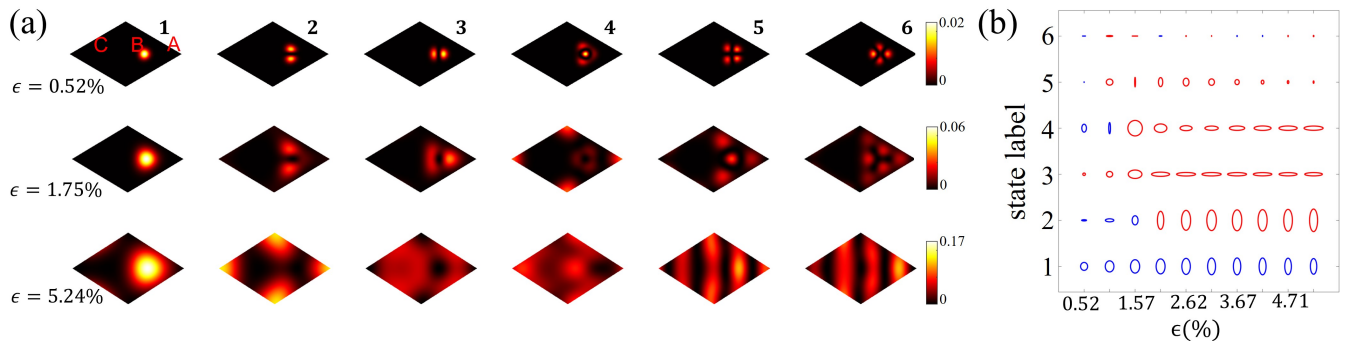


FIG. 6. (a) Wave functions of the first 6 lowest states of moiré excitons in volume-preserving heterostrained moiré along the zigzag direction. The wave functions' three-fold rotational symmetry is broken, while the mirror symmetry along the long-axis of the moiré unit cell remains. (b) The in-plane polarization of strain moiré excitons from $\epsilon = 0.52\%$ to 5.2% . Red/blue color stands for positive/negative helicities, ellipse size stands for dipole amplitude.

by studying the volume-preserving strain. From discussions in Sec. IV A, we know that strain shifts Dirac cones away from BZ corners. Thus, the kinetic momentum in Eq. (3) should be replaced by

$$\mathbf{Q}_l^s = \mathbf{Q}_l + \mathbf{A} \quad (8)$$

in the presence of strain. Fig. 5a shows the distribution of light cones in volume-preserving strained moiré, where the brown arrow denotes the shift caused by the gauge potential \mathbf{A} with respect to the origin (brown dot). Interestingly, here the size of \mathbf{A} is almost identical to the length of the mini BZ boundary, which results in the following redistribution of the light cones. C_3 symmetry of the three main light cones is broken, which is manifested on the exchange of the dipole polarization of the two main light cones on the two sides of the yellow arrow in Fig. 1c³⁰. In contrast to the twisting case in Fig. 2a, the three main light cones are no longer sitting on the same equi-energy circle (smaller ring in Fig. 5a), with one of them shifted to higher energy (larger ring). Meanwhile, one of the 1st Umklapp light cones moves towards the origin and stays close to the smaller equi-energy circle. As will be shown later, this change will suppress the optical strength of the low energy states.

Now we look at the effects of heterostrain on the dispersion of IXs. Fig. 5b shows the exciton dispersion without the moiré potential along the direction marked by the black dashed line in Fig. 5a. The first (approximate) degeneracy at Γ consists of two degenerate main light cones and a 1st Umklapp light cone with slightly different energy. The second level at Γ originates from the remaining main light cone and the third level comprises of two degenerate 2nd Umklapp light cones (pink stars near the larger ring in Fig. 5a). Such redistribution of main and Umklapp light cones among the states, as compared to the case of twisting (Fig. 3a), will yield distinct optical properties.

For different types of moiré superlattices, e.g., twisting vs heterostrain, the moiré potential is only affected via changes of moiré primitive reciprocal lattice vectors

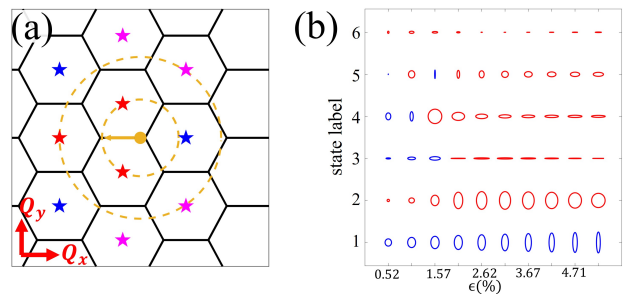


FIG. 7. Moiré excitons from volume-preserving heterostrain along the armchair direction. (a) The light cone distribution. Black hexagons denote the moiré BZs. Red and blue/pink stars represent main and 1st/2nd Umklapp light cones. The brown dot, arrow and dashed circles represent the origin, gauge potential \mathbf{A} , and equi-energy rings, respectively. (b) The in-plane polarization of strain moiré excitons from $\epsilon = 0.52\%$ to 5.2% . Red/blue color stands for positive/negative helicities, ellipse size stands for dipole amplitude.

(Eq. (2)). This only changes the spatial profile instead of the magnitude of the moiré potential. Analogous to the twisting case, momentum eigenstates in different moiré BZs are coupled through the Fourier components of the moiré potential. On the other hand, the kinetic energy is affected by the strain-induced pseudogauge potential and – different from the twisting case – \mathbf{Q}_l should be replaced by \mathbf{Q}_l^s in Eq. (3) for strained moiré excitons. The mini-bands in the presence of moiré potential is shown in Fig. 5c, which resembles that of the twisted moiré (Fig. 3b).

Such similarity extends to the evolution of energy levels at Γ versus the variation of ϵ or θ (Fig. 5d). This is because energy levels only depend on strength of moiré potential and the distribution of light cones irrespective of their nature (main or Umklapp)⁴².

Instead, different distributions of light cones between the heterostrain and twisting cases are reflected on the

wave functions (Fig. 6a). In general, the local densities of the wave functions lose three-fold rotational symmetry. However, the mirror symmetry with respect to the long axis of the supercell is retained. Despite changes in symmetry, the features of spatial distribution remain unchanged: For small strain strength, wave functions exhibit local orbital features at potential minima; For large strain strength, wave functions exhibit extended Bloch wave forms, where quasi-1D stripe patterns can be spotted for high energy states.

The optical properties of strained moiré excitons are also remarkably distinct from the twisted ones (Fig. 6b). Compared with twisted excitons, one finds: (i) The first four states at Γ possess comparable dipole strength independent of strain intensity. While for twisted moiré excitons, the first two states possess prominent dipole strength, especially at large twist angles (Fig. 4d); (ii) The 3rd and 6th states have finite dipole strength in contrast to the vanishing contributions in the case of twisting; (iii) The coupled light in strained moiré is elliptically instead of circularly polarized. The first difference results from the light cone redistribution. As is shown in Fig. 5b, the lower states at Γ point are composed of two main light cones and one 1st Umklapp light cone, while the higher states comprise of two 2nd Umklapp light cones and one main light cone. The average effects of strong and weak dipoles from main and Umklapp light cones make the first 4 states exhibit comparable dipole strengths. The second and third differences can be attributed to the distinct symmetry properties. The breaking of three-fold rotational symmetry leads to optical dipole with left and right circular polarization of different strengths, thus forming elliptically polarized light. Notice that the 3rd state still locates around C locals at $\epsilon = 5.24\%$ (Fig. 6a), however, the symmetry breaking at C locals ensures that in-plane polarized light-matter coupling is permitted, in contrast to the twisting case. While for the 6th state, its strip-like distribution spread across different locals, which leads to the finite in-plane dipole as compared to its vanishing counterpart in twisted moiré. Similar to the case of twisting, the change of the ordering of the plateau state is also reflected in the optical properties between the 4th and 5th states for strained moiré excitons.

One can also apply the volume-preserving strain along the armchair direction with the strain tensor $S = \text{diag}(-\epsilon, \epsilon)$. The light cone distribution exhibits an approximate mirror reflection in the \mathbf{Q}_y direction compared with the above case (Fig. 7a vs Fig. 5a). Such relation in the light cone distribution guarantees that the optical dipoles in the two cases are similar (Fig. 7b vs Fig. 6b).

C. Uniaxial strain

In this section we consider moiré formed from uniaxial heterostrain along the zigzag direction. The strain tensor reads $S = \text{diag}(\epsilon, -\nu\epsilon)$, where the Poisson ratio $\nu = 0.19$ for WSe_2 ⁴³. This geometry allows us to explore the in-

terplay of the effects of strong geometric distortion and the pseudo-gauge potential. Due to the different deformations along zigzag and armchair directions, the moiré superlattice geometry is changed significantly compared to that of a twisted or volume-preserving strained bilayer. The supercell is compressed along the short axis, forming strip-like supercells (Fig. 8a).

The mini BZ is also deformed dramatically, which affects the location of Dirac cones significantly and redistributes the light cones in a very different manner (Fig. 8d). A main light cone is shifted away from the origin. Besides, two of the 2nd Umklapp light cones (pink stars) stay much closer to the origin. All the light cones are close to each other in the \mathbf{Q}_y direction but become well separated along \mathbf{Q}_x . In the presence of moiré potential, light cones along \mathbf{Q}_y are expected to be strongly coupled. Compared with volume-preserving strain, the valley mismatch becomes smaller for uniaxial strain. This results in an overall lowering of the energy levels and band hybridization mediated by the plateau state is absent within the studied energy range since the plateau state has higher energy (Fig. 8e).

As for wave function distribution, the first six states all locate around B locals (Fig. 8b). Their profiles are analogous to the eigenstates of a 1D harmonic oscillator, as the potential minima are compressed to strips. Such strip-like features is a manifestation of the strong coupling between the light cones along \mathbf{Q}_y direction due to the compression in the momentum space.

The light cone redistribution also affects optical properties. Since one of the main light cones is away from the origin, and there is a mixture of main and Umklapp light cones at both low and high energies near the two equi-energy circles (Fig. 8d), the first six states exhibit comparable dipole strength (Fig. 8f). Besides, all the eigenstates, except the ground state, are contributed by distinct light cone combinations from the case of volume-preserving strain. For the ground state that has the similar optical dipole constituent with the case of volume-preserving strain, the compressed short axis in the supercell dictates that the vertically orientated elliptical polarization becomes narrower and more linear-like (cf. Fig. 6b).

D. General strain tuning

In principle, strain can be tuned independently along the two axes. To explore the effects of strain on the optical properties of moiré IXs more systematically, we tune the two strain components ϵ_{xx} and ϵ_{yy} continuously from volume-preserving ($\epsilon_{xx} = -\epsilon_{yy}$) to biaxial ($\epsilon_{xx} = \epsilon_{yy}$) configuration. Fig. 9 shows the diagrams on the optical properties of the first three states of moiré IXs at Γ in the strain-parameter space. The blank areas on the diagram correspond to the situations where the superlattices become quasi-1D with gigantic periods, thus the results are not provided due to numerical limitations.

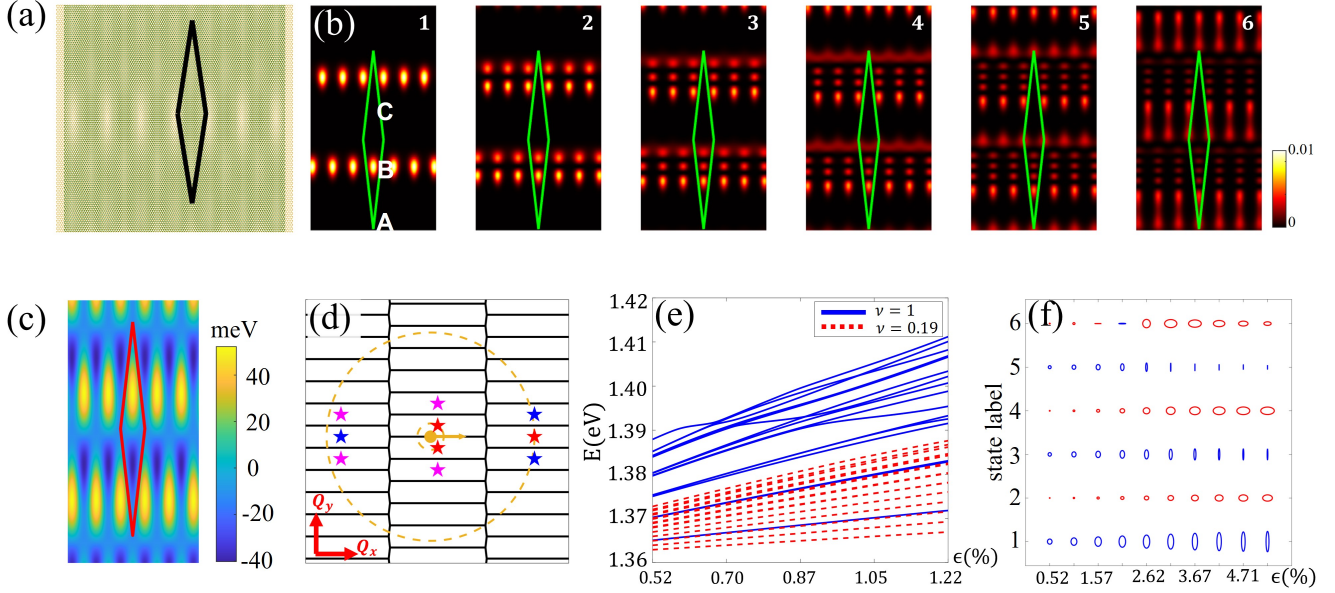


FIG. 8. Moiré excitons from uniaxial heterostrain. (a) Real-space lattice of a heterobilayer, where yellow/green atoms are from the upper/lower layer. Black rhombus depicts the moiré supercell. (b) Wave function densities of the first six lowest states at $\epsilon = 3.5\%$. Green rhombuses mark the supercells. (c) The moiré potential. (d) The light cone distribution. Black lines depict the moiré BZ boundaries. Red and blue/pink stars represent main and 1st/2nd Umklapp light cones. The brown dot, arrow and dashed circles represent the origin, gauge potential \mathbf{A} , and equi-energy rings, respectively. (e) Comparison of energy levels at Γ from volume-preserving strain (blue) and uniaxial (red dashed) strain. (f) The in-plane polarization of the first six lowest states. (g)-(i) The in-plane polarization of the first three states in case of general ϵ_{xx} and ϵ_{yy} . In (f)-(i), red/blue color stands for positive/negative helicities, ellipse size stands for dipole amplitude.

The upper three panels describe the amplitude of dipoles, where positive (negative) values indicate that the semi-major axis of an elliptical polarization is parallel (perpendicular) to the x axis. The lower three panels describe the ellipticity angle of the polarization, where $\pm 45^\circ$ corresponds to σ_{\pm} circular polarization. The two yellow dashed lines in the first panel correspond to the cases of uniaxial strain with $\epsilon_{yy} = -\nu\epsilon_{xx}$ and $\epsilon_{xx} = -\nu\epsilon_{yy}$, where $\nu = 0.19$. The two diagonal directions in each panel describe the cases of volume-preserving and biaxial strain, respectively. In particular, a biaxially strained bilayer, whose pseudo-gauge potential vanishes, resembles a lattice-mismatched heterobilayer. Consequently, the optical properties of the former case can be employed to qualitatively understand those of the latter. Furthermore, due to similar moiré landscapes with identical symmetries, a biaxially strained bilayer and a twisted bilayer with equal moiré period share the identical in-plane polarization (cf. Fig. 4d).

E. Mixture of twisting and heterostrain

In this section, we briefly discuss the mixture of twisting and heterostrain. In general, the strain and rotation operators do not commute. Also, the mixture of twisting and heterostrain will deform the BZ nontrivially, which makes the problem quite complicated. In the follow-

ing, we illustrate the effects of the interplay by applying volume-preserving strain along the zigzag direction to the top layer followed by twisting.

Fig. 10a illustrates the evolution of the moiré potential landscape by fixing the twist angle while changing the strength of strain. When the size of strain is enlarged and approaches the twist angle, the supercell stretches and becomes a 1D strip gradually. Dirac cones in the two layers are separated in a more complicated manner in the presence of nontrivially distorted BZ and the pseudogauge potential due to the superposition of twisting and strain. This results in a redistribution of the light cones that affects the wave function distribution as well as the optical properties.

Fig. 10b shows the wave function distribution of the three lowest states at Γ in different mixtures. Although they still exhibit localization around potential extrema at the high symmetry locals, their profiles become irregular due to the lack of both C_3 rotation and mirror symmetry.

When $\epsilon \leq 1.05\%$, the three main light cones maintain approximate degeneracy, so the two lowest states exhibit dominant optical dipole strength (Figs. 10c, d). As strain is increased and approaches the size of the twist angle, main light cones are more separated and shifted toward high energy states (Fig. 10e). Thus, high energy states can be tuned to exhibit dominant dipole strength with strain engineering (Fig. 10c).

Strain can also be unintentionally introduced in de-

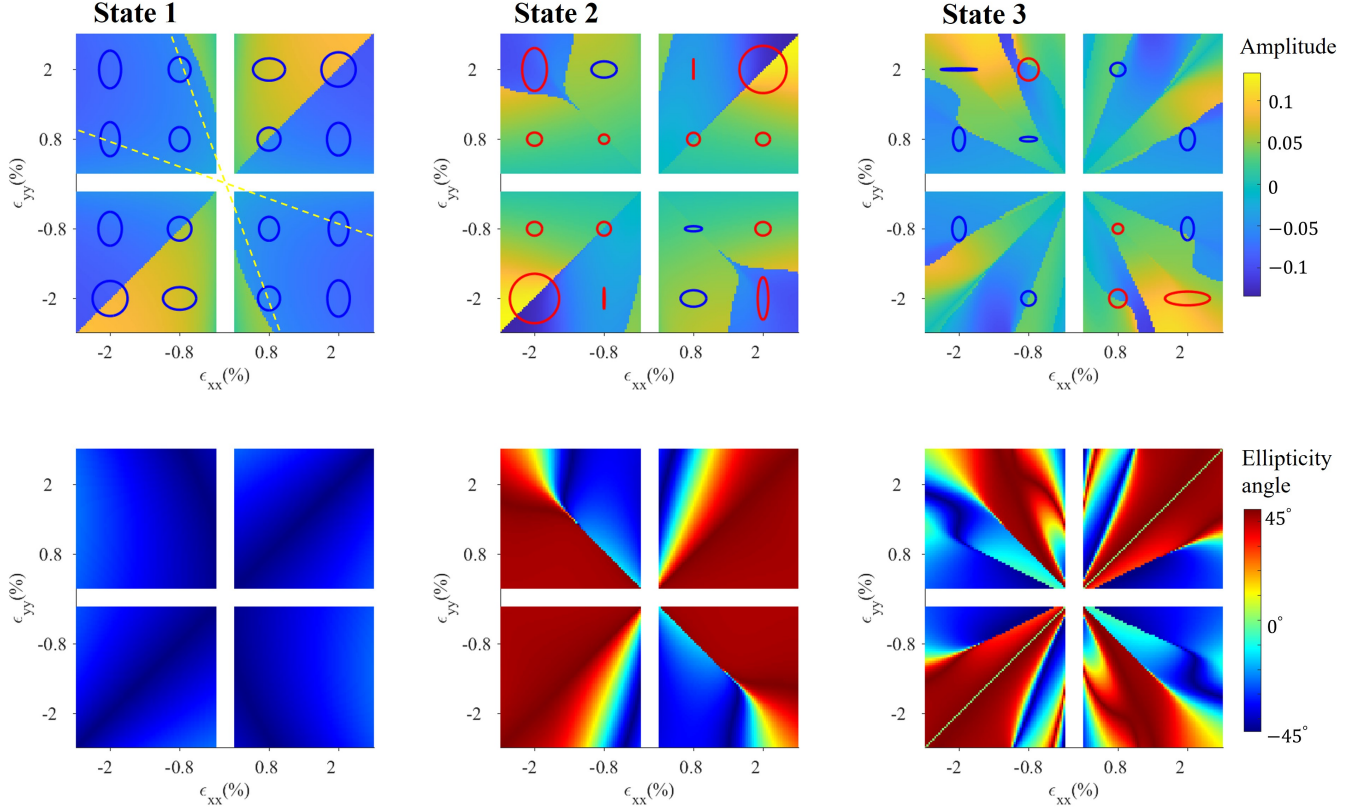


FIG. 9. Diagrams of IXs optical properties with strain tuning. The upper three panels describe the dipole amplitude, which is measured in units of the dipoles of intralayer exciton. Positive (negative) value represents that the semi-major axis of an elliptical polarization is parallel (perpendicular) to the x axis. The two yellow dashed lines in the first panel correspond to $\epsilon_{yy} = -\nu\epsilon_{xx}$ and $\epsilon_{xx} = -\nu\epsilon_{yy}$, where $\nu = 0.19$. The lower three panels describe the ellipticity angle of polarization, where $\pm 45^\circ$ stands for σ_{\pm} circular polarization. Results along $\epsilon_{xx} = \epsilon_{yy}$ in the last panel are meaningless as in-plane polarization vanishes. Some specific dipole polarizations are marked as rings in the upper panel, where the center corresponds to the strain configuration, the size represents the amplitude, and red/blue color indicates positive/negative helicity.

vice fabrications, which can have a general intensity and direction⁴¹. In Appendix B we provide diagrams of optical properties of moiré IXs in a moiré with a fixed twist angle but arbitrary strain intensity and direction, i.e., $S = \epsilon \begin{pmatrix} \cos 2\phi & \sin 2\phi \\ \sin 2\phi & -\cos 2\phi \end{pmatrix}$, where the strain direction ϕ is defined by the angle between stretching direction and x axis (Figs. 12 and 13). Such diagrams might be utilized as a toolbox for strain estimation based on optical measurements.

V. SUMMARY

To summarize, we investigate the evolution of wave function and optical properties of interlayer excitons in the moiré formed by different twist angles and heterostrain strength. The wave function evolution is subject to local atomic alignments and the light cone distribution. In the small twist angles or strain strength regime, densely arranged light cones dictate that wave functions are localized orbitals and optical selection rules

are orbital-dependent. While in the opposite limit, sparsely arranged light cones determine that wave functions are extended Bloch-like. This results in various states possessing different rotation centers, consequently, the location-dependent optical selection rules.

Compared with twisted moiré, low-energy carriers in heterostrained moiré are additionally affected by distorted BZ and an effective gauge potential in the momentum space, so that moiré excitons possess distinct wave functions and exhibit elliptically polarized optical selection rules. Due to the redistribution of light cones and 1D stripe-like wave functions in various strain configurations, high energy states can be tuned to exhibit strong optical properties. These results show that strain engineering can be utilized to manipulate light cone distribution and control the optical properties of moiré excitons.

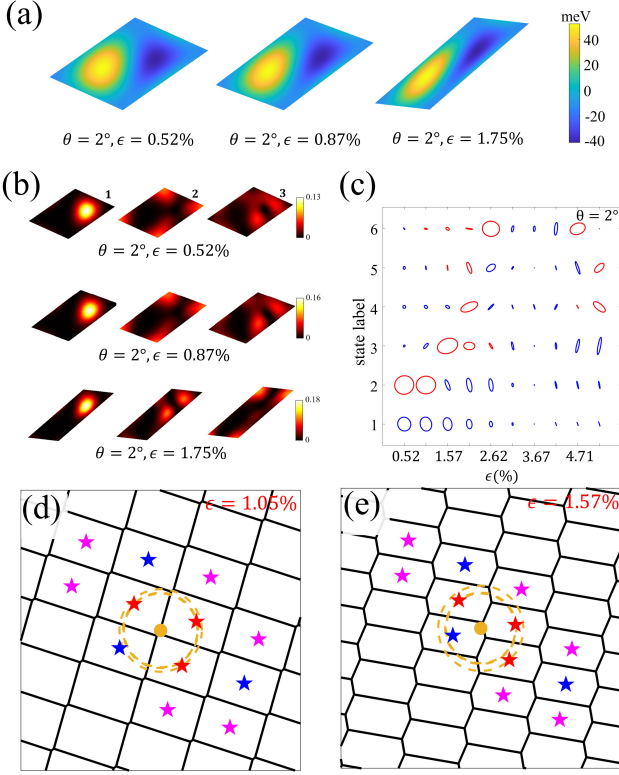


FIG. 10. Moiré excitons from the mixture of twisting and volume-preserving strain. (a) Moiré potential landscape with fixed $\theta = 2^\circ$ while setting $\epsilon = 0.52\%$, 0.87% , 1.75% , respectively. The unit cell deforms as the strain strength approaches the size of the twist angle. (b) Wave functions of the first three states under the same conditions as (a). (c) The in-plane polarization of moiré excitons with fixed twist angle (2°) and different strain intensity. Red/blue color stands for positive/negative helicities, ellipse size stands for dipole amplitude. (d) Light cone distribution at $\theta = 2^\circ$ and $\epsilon = 1.05\%$. Black lines depict the moiré BZ boundaries. Red and blue/pink stars represent main and 1st/2nd Umklapp light cones. The brown dot and dashed circles represent the origin and equi-energy rings, respectively. (e) Light cone distribution at $\theta = 2^\circ$ and $\epsilon = 1.57\%$.

Appendix A: The similarity of potentials in twisted and heterostrained moiré

Our studies are focused on long-wavelength moiré pattern, and the similarity in the superlattice potentials in the two types of moiré is in the context of the low energy electron and hole (and exciton as their composite particle), which can be described well by the local approximation. In such moiré, the period is much larger than the lattice constant of the building block, and there exists an intermediate length scale l , large compared to monolayer lattice constant, but small compared to moiré period a_m . A local region of size l encloses sufficient number of monolayer unit cells, whereas the interlayer atomic registry can be considered nearly uniform within this local region (as the spatial variation occurs on the

scale $a_m \gg l$), where the local electronic structure can be well approximated by that of the lattice-matched bilayers with the corresponding interlayer registry.

The modelling of the moiré superlattices is based on such local approximations. The first step is to establish the mapping between the spatial location \mathbf{R} in the moiré supercell and the local interlayer atomic registry \mathbf{d} . The mapping functions depend on the twisting between the layers, applied strain, and differences in lattice constants of the building blocks through \mathbf{d} . In the second step, one examines first principle calculated electronic structures of lattice-matched bilayers with various interlayer registries \mathbf{d} , and extracts the \mathbf{d} dependence of the local properties, which, combined with the mapping $\mathbf{d}(\mathbf{R})$, will establish the moiré superlattice models. This approach based on the local approximation has been successfully implemented and validated in the studies of moiré superlattices.

In the following, we show explicitly the similarity between the mapping functions $\mathbf{d}(\mathbf{R})$ of the twisted moiré and the moiré from volume-preserving strain, thus similarity in their moiré potential landscapes. At an arbitrary location (x, y) , for twisted bilayer, $\mathbf{d} \approx \theta(y^{(\theta)}, -x^{(\theta)})$, where the superscripts indicate the origin of the moiré. For heterostrained bilayer, $\mathbf{d} \approx \theta(-x^{(\epsilon)}, y^{(\epsilon)})$ if volume-preserving strain is applied. One can easily identify that there is a one-to-one correspondence between locations in the two moiré superlattices, i.e., at $x^{(\epsilon)} = -y^{(\theta)}$ and $y^{(\epsilon)} = -x^{(\theta)}$, where the displacements become equivalent (Fig. 11a). Because of these correspondence in the two mapping functions $\mathbf{d}(\mathbf{R})$ (Fig. 11b), within the local approximation, the moiré potentials landscapes in the two cases differ by a 90° rotation (Fig. 11c). We shall also note a subtle difference: the supercell of a twisted bilayer is a rhombus whose four sides are separated by 60° or 120° , while the angles in a volume-preserving strained moiré can be slightly different, but the difference is negligible in the limit of large moiré period.

In addition, the dependence of moiré potential on interlayer atomic registry \mathbf{d} can be transformed into an equivalent form that depends on the primitive reciprocal lattice vectors of the moiré superlattice, i.e., $\mathbf{G}_n \cdot \mathbf{d} = \mathbf{g}_n \cdot \mathbf{R}$, where \mathbf{G}_n is the primitive reciprocal lattice vectors of monolayer lattices. This format has been used in the main text (Eq. 2), where different moiré lattices are distinguished by the distinct reciprocal lattice vectors,

The above local approximation also applies to moiré superlattices formed from other types of heterostrain or combined effects of strain and twisting. In such cases, the moiré realizes elongated hexagonal lattices (e.g. Fig. 8), where the moiré potential landscapes can also be described by Eq. (2).

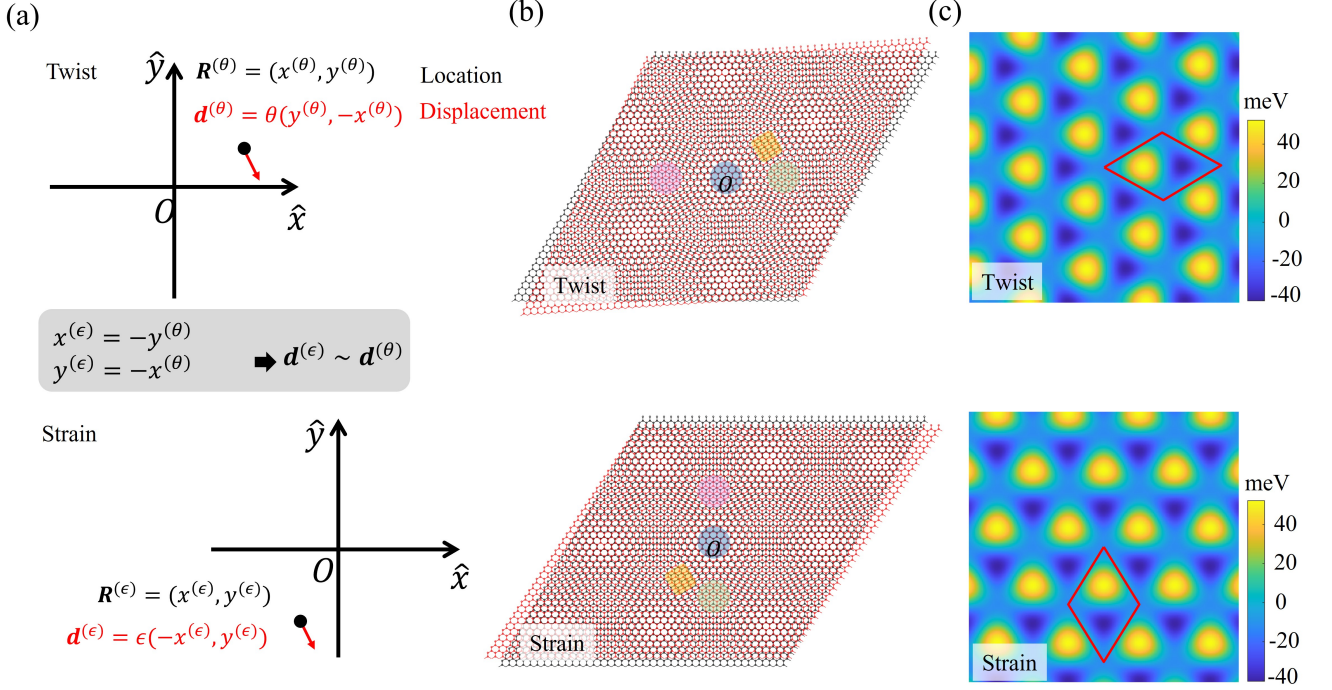


FIG. 11. (a) Relation of the local interlayer displacements in twisted (upper panel) and volume-preserving strained (lower panel) moiré. A one-to-one correspondence exists between the two cases, where the local displacements (red arrows) are equivalent at two locations (black dot) in the superlattices. (b) The correspondence of the interlayer displacements results in a mapping of the local lattice-matched stacking areas in the two superlattices as represented by the shaded regions. (c) Moiré potentials in twisted and volume-preserving strained moiré. The potentials appear to be identical up to a 90° rotation as dictated by the correspondence of the interlayer displacements.

Appendix B: Optical diagram of moiré IXs for mixture of twisting and heterostrain

Here we present the optical diagram of IXs in moiré introduced by mixture of twisting and volume-preserving heterostrain. The strain tensor reads $S = \epsilon \begin{pmatrix} \cos 2\phi & \sin 2\phi \\ \sin 2\phi & -\cos 2\phi \end{pmatrix}$, where the strain direction ϕ is defined as the angle between stretching direction and the x axis. Fig. 12 considers the small twisting angle regime ($\theta = 0.5^\circ$), where strain is varied with strength $0 \leq \epsilon \leq 1.75\%$ and direction $0^\circ \leq \phi \leq 180^\circ$. Since the moiré pattern becomes quasi-1D when $\epsilon \approx \theta$, results for $0.79\% \leq \epsilon \leq 0.96\%$ are not shown. One can see that the dipole amplitude and ellipticity (first two rows of Fig. 12) exhibit a periodicity of 60° with respect to ϕ . Although not obvious, one can verify that the orientation angle (third row of Fig. 12) modulo 60° also shows the same periodicity. Such periodicity originates from the three-fold rotational symmetry (C_3) of TMDs: The crystalline

structure in the region $0^\circ \sim 60^\circ$ is equivalent to that in $120^\circ \sim 180^\circ$ by C_3 . While applying strain in the region $60^\circ \sim 120^\circ$ is identical to that in $-120^\circ \sim -60^\circ$, which is also equivalent to $0^\circ \sim 60^\circ$ by C_3 (see schematics in Fig. 12). When strain is small, effects of twisting dominates, which is reflected in the circular polarization of the first state. As strain is enlarged, state exchange happens between the 2nd and the 3rd states, which is represented by the emergence of some boundaries in the diagram (e.g. black dashed curves in the middle panel). Similarly, Fig. 13 considers the regime of large twisting angle ($\theta = 2^\circ$) with strain strength $0 \leq \epsilon \leq 2.62\%$ and direction $0^\circ \leq \phi \leq 180^\circ$.

ACKNOWLEDGMENTS

The authors thank Hongyi Yu for helpful discussions. The work is support by the National Key R&D Program of China (2020YFA0309600), the Research Grant Council of Hong Kong (AoE/P-701/20), and the Croucher Senior Research Fellowship.

¹ K. F. Mak, C. Lee, J. Hone, J. Shan, and T. F. Heinz, *Phys. Rev. Lett.* **105**, 136805 (2010).

² A. Splendiani, L. Sun, Y. Zhang, T. Li, J. Kim, C.-Y. Chim, G. Galli, and F. Wang, *Nano Lett.* **10**, 1271 (2010).

- ³ H. Yu, X. Cui, X. Xu, and W. Yao, *Natl. Sci. Rev.* **2**, 57 (2015).
- ⁴ P. Rivera, J. R. Schaibley, A. M. Jones, J. S. Ross, S. Wu, G. Aivazian, P. Klement, K. Seyler, G. Clark, N. J. Ghimire, J. Yan, D. G. Mandrus, W. Yao, and X. Xu, *Nat. Commun.* **6**, 6242 (2015).
- ⁵ Y. Gong, J. Lin, X. Wang, G. Shi, S. Lei, Z. Lin, X. Zou, G. Ye, R. Vajtai, B. I. Yakobson, H. Terrones, M. Terrones, B. K. Tay, J. Lou, S. T. Pantelides, Z. Liu, W. Zhou, and P. M. Ajayan, *Nat. Mater.* **13**, 1135 (2014).
- ⁶ F. Ceballos, M. Z. Bellus, H.-Y. Chiu, and H. Zhao, *ACS Nano* **8**, 12717 (2014).
- ⁷ H. Fang, C. Battaglia, C. Carraro, S. Nemsak, B. Ozdol, J. S. Kang, H. A. Bechtel, S. B. Desai, F. Kronast, A. A. Unal, G. Conti, C. Conlon, G. K. Palsson, M. C. Martin, A. M. Minor, C. S. Fadley, E. Yablonovitch, R. Maboudian, and A. Javey, *Proc. Natl. Acad. Sci. U.S.A.* **111**, 6198 (2014).
- ⁸ P. Rivera, K. L. Seyler, H. Yu, J. R. Schaibley, J. Yan, D. G. Mandrus, W. Yao, and X. Xu, *Science* **351**, 688 (2016).
- ⁹ Y.-C. Lin, R. K. Ghosh, R. Addou, N. Lu, S. M. Eichfeld, H. Zhu, M.-Y. Li, X. Peng, M. J. Kim, L.-J. Li, R. M. Wallace, S. Datta, and J. A. Robinson, *Nat. Commun.* **6**, 7311 (2015).
- ¹⁰ C. Zhang, C.-P. Chuu, X. Ren, M.-Y. Li, L.-J. Li, C. Jin, M.-Y. Chou, and C.-K. Shih, *Sci. Adv.* **3**, e1601459 (2017).
- ¹¹ Q. Wang, S. Kishimoto, and Y. Yamauchi, *Opt. Lett.* **37**, 548 (2012).
- ¹² H. Yu, G.-B. Liu, J. Tang, X. Xu, and W. Yao, *Sci. Adv.* **3**, e1701696 (2017).
- ¹³ K. L. Seyler, P. Rivera, H. Yu, N. P. Wilson, E. L. Ray, D. G. Mandrus, J. Yan, W. Yao, and X. Xu, *Nature* **567**, 66 (2019).
- ¹⁴ K. Tran, G. Moody, F. Wu, X. Lu, J. Choi, K. Kim, A. Rai, D. A. Sanchez, J. Quan, A. Singh, J. Embley, A. Zepeda, M. Campbell, T. Autry, T. Taniguchi, K. Watanabe, N. Lu, S. K. Banerjee, K. L. Silverman, S. Kim, E. Tutuc, L. Yang, A. H. MacDonald, and X. Li, *Nature* **567**, 71 (2019).
- ¹⁵ C. Jin, E. C. Regan, A. Yan, M. Iqbal Bakti Utama, D. Wang, S. Zhao, Y. Qin, S. Yang, Z. Zheng, S. Shi, K. Watanabe, T. Taniguchi, S. Tongay, A. Zettl, and F. Wang, *Nature* **567**, 76 (2019).
- ¹⁶ E. M. Alexeev, D. A. Ruiz-Tijerina, M. Danovich, M. J. Hamer, D. J. Terry, P. K. Nayak, S. Ahn, S. Pak, J. Lee, J. I. Sohn, M. R. Molas, M. Koperski, K. Watanabe, T. Taniguchi, K. S. Novoselov, R. V. Gorbachev, H. S. Shin, V. I. Fal'ko, and A. I. Tartakovskii, *Nature* **567**, 81 (2019).
- ¹⁷ M. Brotons-Gisbert, H. Baek, A. Molina-Sánchez, A. Campbell, E. Scerri, D. White, K. Watanabe, T. Taniguchi, C. Bonato, and B. D. Gerardot, *Nat. Mater.* **19**, 630 (2020).
- ¹⁸ W. Li, X. Lu, S. Dubey, L. Devenica, and A. Srivastava, *Nat. Mater.* **19**, 624 (2020).
- ¹⁹ Y. Zhang, Y. Kim, M. J. Gilbert, and N. Mason, *Appl. Phys. Lett.* **115**, 143508 (2019).
- ²⁰ H. Yu, M. Chen, and W. Yao, *Natl. Sci. Rev.* **7**, 12 (2020).
- ²¹ D. Zhai and W. Yao, *Phys. Rev. Mater.* **4**, 094002 (2020).
- ²² R. Frisenda, M. Drüppel, R. Schmidt, S. Michaelis de Vasconcellos, D. Perez de Lara, R. Bratschitsch, M. Rohlfing, and A. Castellanos-Gomez, *NPJ 2D Mater. Appl.* **1**, 10 (2017).
- ²³ R. Roldán, A. Castellanos-Gomez, E. Cappelluti, and F. Guinea, *J. Phys. Condens. Matter* **27**, 313201 (2015).
- ²⁴ S. Deng, A. V. Sumant, and V. Berry, *Nano Today* **22**, 14 (2018).
- ²⁵ S. Yang, Y. Chen, and C. Jiang, *InfoMat* (2021).
- ²⁶ Y. Han, J. Zhou, H. Wang, L. Gao, S. Feng, K. Cao, Z. Xu, and Y. Lu, *Appl. Nanosci.* **11**, 1075 (2021).
- ²⁷ Y. Bai, L. Zhou, J. Wang, W. Wu, L. J. McGilly, D. Halbertal, C. F. B. Lo, F. Liu, J. Ardelean, P. Rivera, N. R. Finney, X.-C. Yang, D. N. Basov, W. Yao, X. Xu, J. Hone, A. N. Pasupathy, and X.-Y. Zhu, *Nat. Mater.* **19**, 1068 (2020).
- ²⁸ G.-B. Liu, D. Xiao, Y. Yao, X. Xu, and W. Yao, *Chem. Soc. Rev.* **44**, 2643 (2015).
- ²⁹ H. Yu, G.-B. Liu, and W. Yao, *2D Mater.* **5**, 035021 (2018).
- ³⁰ H. Yu, Y. Wang, Q. Tong, X. Xu, and W. Yao, *Phys. Rev. Lett.* **115**, 187002 (2015).
- ³¹ Y. Wang, Z. Wang, W. Yao, G.-B. Liu, and H. Yu, *Phys. Rev. B* **95**, 115429 (2017).
- ³² F. Wu, T. Lovorn, and A. H. MacDonald, *Phys. Rev. B* **97**, 035306 (2018).
- ³³ H. Yu and W. Yao, *Sci. Bull.* **65**, 1555 (2020).
- ³⁴ F. Wu, T. Lovorn, and A. H. MacDonald, *Phys. Rev. Lett.* **118**, 147401 (2017).
- ³⁵ Strain can be induced by various methods, such as pulling on suspended sheets with an electrostatic gate, or by bending a flexible substrate^{22–26}. In experiments, errors/uncertainties may occur when applying strain to the samples. First, not all the applied strain to the substrate was transferred to the sample^{44,45}. This uncertainty can be calibrated by measuring strain transfer efficiency. Besides, strain distribution might be nonuniform due to interactions between the substrate and the sample. Experimentally, strain with uncertainty < 0.1% in a few microns' scale can be achieved^{44,46}. The optical properties of interlayer excitons usually have no qualitative changes within strain variation of < 0.1% (Fig. 9, with exceptions near transition boundaries).
- ³⁶ M. Vozmediano, M. Katsnelson, and F. Guinea, *Phys. Rep.* **496**, 109 (2010).
- ³⁷ G. G. Naumis, S. Barraza-Lopez, M. Oliva-Leyva, and H. Terrones, *Rep. Prog. Phys.* **80**, 096501 (2017).
- ³⁸ S. Fang, S. Carr, M. A. Cazalilla, and E. Kaxiras, *Phys. Rev. B* **98**, 075106 (2018).
- ³⁹ H. Rostami, R. Roldán, E. Cappelluti, R. Asgari, and F. Guinea, *Phys. Rev. B* **92**, 195402 (2015).
- ⁴⁰ Z. Bi, N. F. Q. Yuan, and L. Fu, *Phys. Rev. B* **100**, 035448 (2019).
- ⁴¹ S. Shabani, D. Halbertal, W. Wu, M. Chen, S. Liu, J. Hone, W. Yao, D. N. Basov, X. Zhu, and A. N. Pasupathy, *Nat. Phys.* **17**, 720 (2021).
- ⁴² The similarity of A and K_m is caused by the material-dependent parameter β . For volume-preserving strain, the $A = \frac{\sqrt{3}\beta}{2a}(\epsilon_{xx} - \epsilon_{yy}) = \frac{\sqrt{3}\beta\epsilon}{a}$, and $K_m = \frac{4\pi}{3a_m} \approx \frac{4\pi\epsilon}{3a}$, where $a_m \approx a/\epsilon$ is moiré period. The ratio of the two quantities becomes $\frac{A}{K_m} = \frac{3\sqrt{3}\beta}{4\pi}$, which only depends on β . The ratio is approximately 0.95 (0.99) for WSe_2 (MoSe_2) whose $\beta = 0.23$ (0.24).
- ⁴³ D. Çakır, F. M. Peeters, and C. Sevik, *Appl. Phys. Lett.* **104**, 203110 (2014).
- ⁴⁴ Z. Liu, M. Amani, S. Najmaei, Q. Xu, X. Zou, W. Zhou, T. Yu, C. Qiu, A. G. Birdwell, F. J. Crowne, R. Vajtai, B. I. Yakobson, Z. Xia, M. Dubey, P. M. Ajayan, and

- J. Lou, *Nat. Commun.* **5**, 5246 (2014).
- ⁴⁵ Z. Li, Y. Lv, L. Ren, J. Li, L. Kong, Y. Zeng, Q. Tao, R. Wu, H. Ma, B. Zhao, D. Wang, W. Dang, K. Chen, L. Liao, X. Duan, X. Duan, and Y. Liu, *Nat. Commun.* **11**, 1151 (2020).
- ⁴⁶ M. Goldsche, J. Sonntag, T. Khodkov, G. J. Verbiest, S. Reichardt, C. Neumann, T. Ouaj, N. von den Driesch, D. Buca, and C. Stampfer, *Nano Lett.* **18**, 1707 (2018).

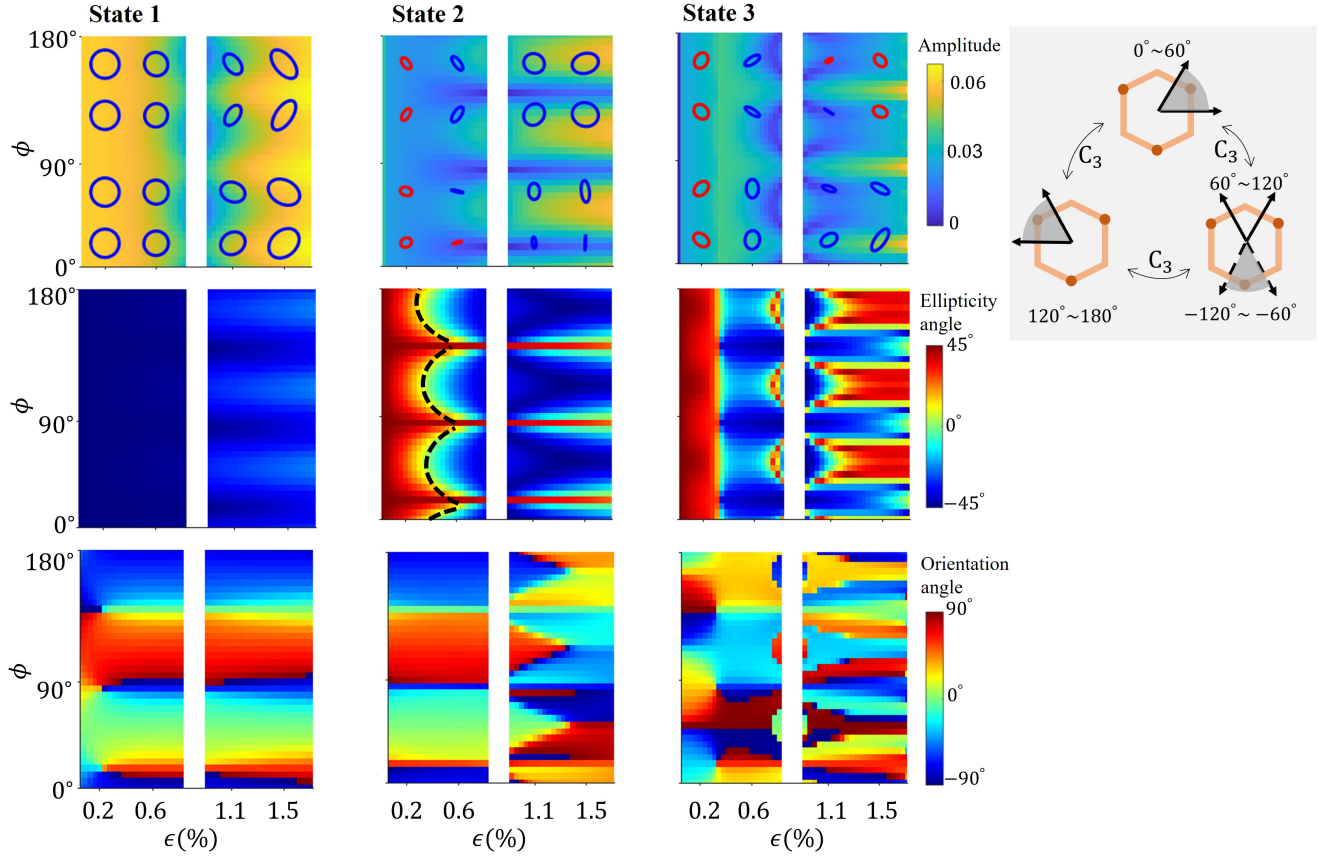


FIG. 12. Diagrams of optical properties of IXs in the moiré induced by a mixture of twisting and heterostrain. Here twist angle is fixed at 0.5° , while the volume-preserving strain has its magnitude varied from 0 to 1.75% and direction from 0° to 180° . The upper three panels describe the dipole amplitude measured in units of the dipoles of intralayer exciton. The middle three panels describe the ellipticity angle of the polarization, where $\pm 45^\circ$ stands for σ_{\pm} circular polarization. The lower three panels describe the orientation angle of the polarization— angle between semi-major axis of elliptical polarization and x axis. Some specific dipole polarizations are marked in the upper panels, where the size of ellipse represents the amplitude and red/blue color indicates positive/negative helicity. The schematics on the right illustrate the equivalence of the three angular regions for applying strain, i.e., $0^\circ \sim 60^\circ$, $60^\circ \sim 120^\circ$, and $120^\circ \sim 180^\circ$. The hexagon stands for a TMD cell and solid black arrows enclose the three angular regions.

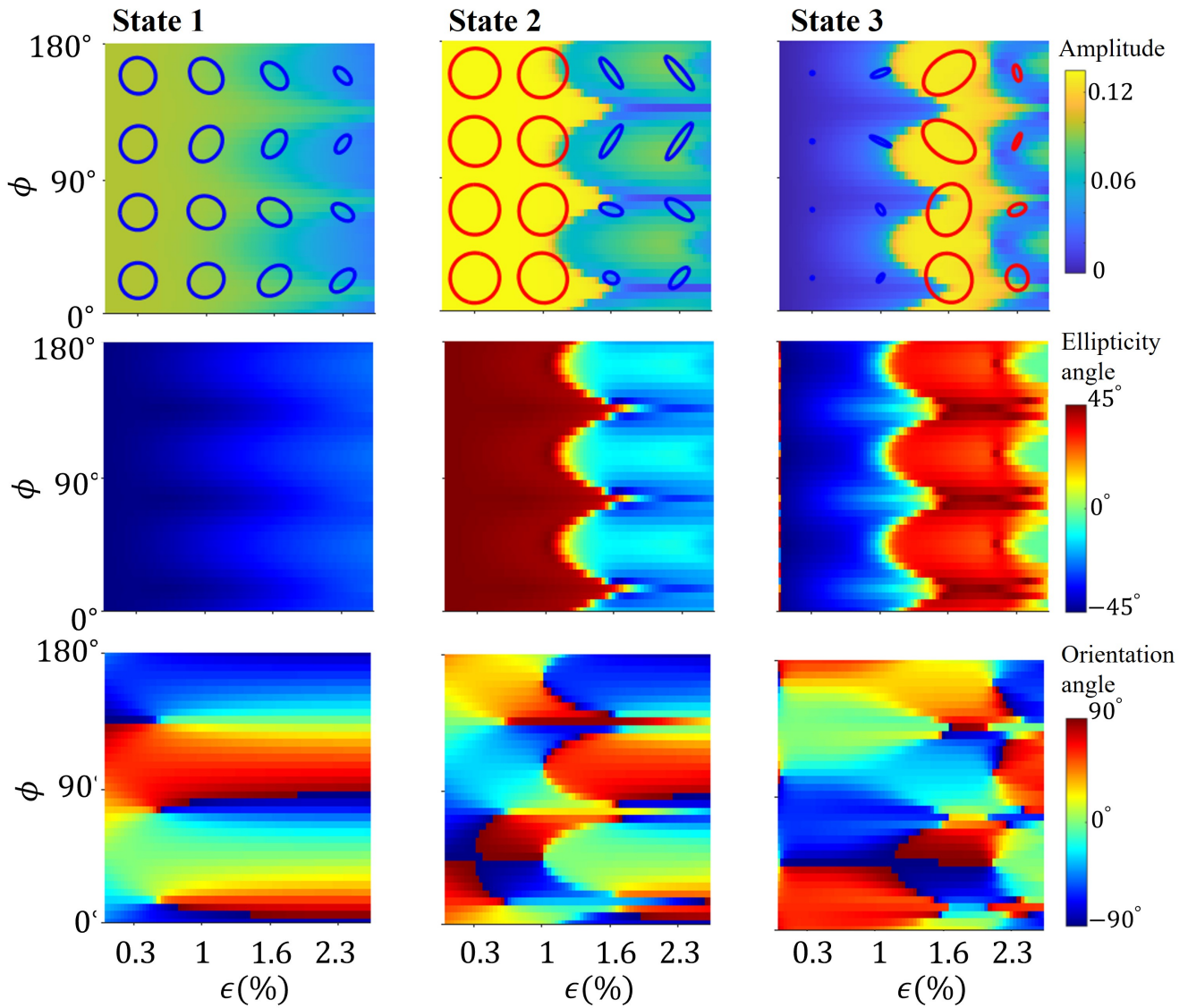


FIG. 13. Same as Fig. 12 but with twist angle equals to 2° and volume-preserving strain whose magnitude varies from 0 to 2.62%, and direction from 0° to 180° .